Row-Column Beamformer for Fast Volumetric Imaging

Lasse Thurmann Jørgensen, Sebastian Kazmarek Præsius, Matthias Bo Stuart, Jørgen Arendt Jensen

Center for Fast Ultrasound Imaging, Department of Health Technology, Technical University of Denmark, DK-2800 Lyngby, Denmark

***Abstract*—This work presents a beamforming procedure that significantly reduces the number of operations when performing volumetric synthetic aperture imaging with row-column addressed arrays (RCAs). The proposed beamformer uses that the image values along the elevation direction of the low-resolution volume (LRV) are approximately constant. It is thus hypothesized that the entire LRV could be reconstructed from a single 2-D cross-section of the LRV. The presented method contains two stages; The first stage beamforms, for each emission, a cross-section using the conventional RCA beamformer. The second stage extrapolates the rest of the image points in the volume from the 2-D cross-sections. Assuming the image volume is covered by 3-D grid coordinates with a size of $N_w \times N_w \times N_z$, i.e., N_w samples along the x- and y-axis and N_z samples along the z-axis, the proposed beamformer reduces the number of mathematical operations by a factor of approximately $NN_w/(NS+N_w)$. Here S is the ratio between the first and second stage axial sampling rate, and N is the receiving aperture's number of channels. Beamforming a $128 \times 128 \times 1024$ volume from data acquired with $N = 128$ receiving channel can thus be achieved with 25.6 times fewer operations, when $S = 4$.**

A 9.23 times increase in the beamforming rate for a $100 \times 100 \times 200$ volume with $S = 2$ was demonstrated on complex data from a $128+128$ Vermon RCA probe. Real-time volumetric beamformation can, with this increase, be performed with a pulse repetition frequency of up to 1804.80 Hz.

The proposed and conventional beamformer's output was visually indistinguishable and, the full width at half maximum (FWHM) and full width at tenth maximum (FWTM) were at most 1.19% larger with the proposed approach.

The proposed beamformer can thus perform volumetric imaging significantly faster than the current approach, with a negligible difference in image quality.

***Index Terms*—Row-column addressed probes, volumetric imaging, synthetic aperture imaging, dual stage beamforming**

I. Introduction

High frame rate 3-D imaging with a broad volumetric coverage can be achieved using 2-D probes and synthetic aperture imaging techniques. However, for most 2-D probe designs, the number of channels, M, increases quadratically with the number of elements, N, in the side-length of the aperture [1]–[3]. This makes it practically impossible to achieve a low F-number at large imaging depths due to manufacturing and processing difficulties. Furthermore, when $M \propto N^2$, even small values of N yield a channel count far exceeding that of the typical 2-D imaging system. Row-column addressed arrays (RCAs) provide a solution to the high channel count by addressing the elements of the 2-D array by rows and columns, and this reduces the total number of channels from N^2 to $N+N$; a factor $N/2$ reduction compared to the fully addressed matrix array [4]–[11]. Alternatively, channel reduction can be achieved through sparse arrays [12]–[17], multiplexing, and micro-beamformation [18]–[21].

The RCA is effectively a 1-D array, with elements elongated in elevation, and it performs volumetric imaging by steering the transmitted waves along the elevation direction using a separate orthogonal 1-D array. This design allows for low complexity volumetric beamforming and the the current row-column delay-and-sum (DAS) beamformer [10] uses the same number of operations per image point as the DAS beamformer used in a 2-D imaging system for a linear 1-D array. This implies that the RCA beamformation can be performed as fast as in the 2-D imaging system, assuming an equal number of elements in receive and emissions. However, the remaining issue is that the volumetric images usually contain far more image points, which places a high demand on the processing unit. In [22] a CUDA (Compute Unified Device Architecture) C/C++ implementation of the RCA beamformer achieved approximately 1 Hz volumetric beamformation with the high-end NVIDIA TITAN V graphics card. Here the volume contained $191 \times 191 \times 76$ complex, single precision image points, the RCA had $N = 192$ channels in receive and the sequence used $N_e = 64$ synthetic aperture emissions to construct the high-resolution volume (HRV). Real-time beamformation is therefore only possible, if the pulse repetition is ≤ 64 Hz, which is two orders of magnitude too slow for e.g. real-time flow estimation [23]. As such, the algorithm is currently not fast enough to perform real-time volumetric beamformation at an usable pulse repetition frequency.

Another issue is image storage and retrieval. This is especially an issue in super-resolution imaging, where tens of thousands of high-resolution volumes can be acquired [24]. In such a case, storing the beamformed volumes can take up terabytes of storage, and accessing the volumes can, depending on the volume size, the number of emissions, and the storage device, be slower than performing the beamformation. Therefore, storing just the channel data can sometimes be the best option for reducing storage usage and increasing the image retrieval rate. However, as stated before, the beamformation process is slow, limiting 3-D imaging for clinical use.

This work presents an RCA beamformation approach, which addresses this issue by significantly reducing the number of calculations per image point. The approach uses that the low-resolution volume (LRV) obtained for each emission has approximately constant image values along the elevation axis.

Thus, it is hypothesized is that the entire 3-D LRV can be obtained from only a cross-section of the LRV. The imaging can be, thus, performed in two stages. In the first stage the LRV cross-section is beamformed using the conventional DAS RCA beamformer. In the second stage, the out-of-plane image values are extrapolated from the cross-section.

Because the second stage processing is independent of the number of channels, the computational complexity for beamforming an $N_w \times N_w \times N_z$ HRV is reduced from $O(NN_w^2N_zN_e)$ to $O(N_w^2N_zN_e)$. Here, N_w and N_z denote the number of samples along the width and height of the volume, and $O(\cdot)$ is the big O notation [25], which describes the proportionality of the run-time relative to the problem size. The approach also provides a compression method for the beamformed volumes, which requires little decompression processing. This is because efficient image storage can also be achieved by only storing the 2-D cross-sections from the first stage. The volumes can subsequently be retrieved, with relatively little processing, using the second stage algorithm.

The presented approach has similarities to synthetic aperture sequential beamformation (SASB) [26]–[29], which has also been described for RCA imaging [30]. However, the main difference is that SASB approximates an image obtained with fixed receive focusing, whereas the presented approach approximates RCA imaging with dynamic focusing, i.e., the imaging approach presented in [10]. The time of flight (ToF) calculations, which forms the foundation of both methods, are thus different. It should also be mentioned that RCA imaging with fixed focusing is still only a concept, and the image quality has yet to be determined. In contrast, RCA imaging with dynamic focusing is well-established and has been applied in numerous published research, including [31]–[38].

The rest of the paper is organized as follows; Section II details the two stages of the proposed beamformer. Section III explains the experimental setup, and Sections IV-V presents and interprets the results.

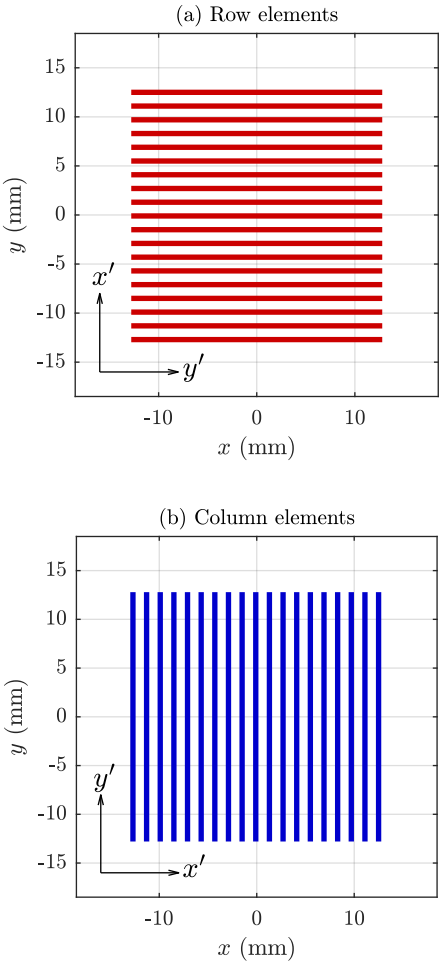

Fig. 1. The x'- and y'-axis relative to the receiving aperture. (a) shows the coordinate system, when the row aperture is the receiving aperture and (b) shows it when the column aperture is the receiving aperture. The blue and red line segments represent the elongated elements of the RCA, and x' is the axis, where the receiving elements are aligned. The orthogonal axis y' is defined as the elements' elevation axis.

II. Proposed imaging method

This section presents the proposed RCA beamformer's two stages and explains the method's underlying hypothesis.

A. First stage algorithm

The proposed beamformer's first stage consists of the conventional RCA DAS beamformer presented in [10]. The ToF equation presented here depends on which aperture isonifies the volume and receives the back-scattered signal. These equations can, however, be generalized by defining the coordinate system relative to the receiving aperture. Let x' denote the axis along the receiving array's elements and let y' denote the axis orthogonal to x' and z, i.e., the elevation axis of the aperture. Note that $(x', y') = (y, x)$ if the row aperture receives, and $(x', y') = (x, y)$ if the column aperture receives the backscattered signal (see Fig. 1). The (x', y', z)-coordinate system thus aligns itself with the receiving aperture, and the equations and coordinates presented in this section are exclusively presented relative to this coordinate system. Let $(x', y', z) = (x_p, y_p, z_p) = \vec{p}$ denote the image point position, $(x', y', z) = (x', y_v, z_v)$ denote the virtual line source position [10] and $(x', y', z) = (x_e, y', 0)$ denote the receiving line element position. Note that the virtual line source is defined such it is always perpendicular to the $y'z$-plane and that the receiving line element is perpendicular to the $x'z$-plane. From the (x', y', z)-coordinate system, the shortest distance from the virtual line source to the image point and back to the receiving element is thus given by

$$d(\vec{p}, x_e) = \begin{cases} z_v - d_v + d_e & \text{if } z_p < z_v \\ z_v + d_v + d_e & \text{otherwise,} \end{cases} \tag{1}$$

where

$$d_v = \sqrt{(y_p - y_v)^2 + (z_p - z_v)^2}, \tag{2}$$

and

$$d_e = \sqrt{(x_p - x_e)^2 + z_p^2}. \tag{3}$$

See Fig. 2 for a visual representation of the shortest path from which this distance is derived, and for further clarification

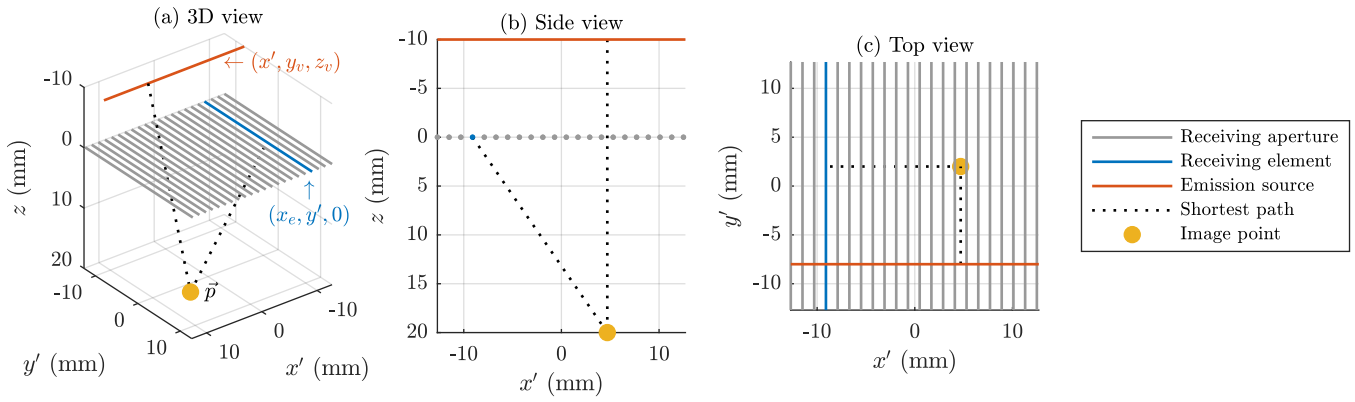

Fig. 2. Shortest path (dashed line) from the virtual line source (red line) to the image point (yellow dot) and back to the receiving line element (blue line) of the RCA probe. This path is used for the ToF calculations in the conventional RCA DAS beamformer and the path's distance correspond to $d_v + d_e$ in (1).

regarding the distance equation, please refer to [10]. With (1) the ToF used in the RCA DAS beamformation is given by $t = d(\vec{p}, x_e)/c$, where c is the speed of sound in the medium.

The ToF equation is identical to the one used in 1-D linear array DAS beamformation, except that the virtual source position is defined on the $y'z$-plane instead of the $x'z$-plane. The RCA can change the virtual source position in the $y'z$-plane by using different oriented apertures in transmit and receive. The RCA is able to resolve objects along the elevation (y'-direction), because it can change the virtual source position in this direction.

Fig. 3 demonstrates how a point target at $(x', y', z) = (0, 0, 20)$ mm is resolved from an RCA emission sequence consisting of $N_e = 22$ unique virtual source positions. Note that the RF-data used to construct the beamformed images shown in this section were all simulated using a 3 MHz $64 + 64$ RCA and Field II [39], [40]. Fig. 3a shows the LRV beamformed from the first emission, where the virtual source line is placed at $(x', y', z) = (x', -5.4, -5.4)$ mm. Fig. 3b shows the LRV from the 22nd emission, where the virtual source line is placed at $(x', y', z) = (x', 5.4, -5.4)$ mm, and Fig. 3c shows the resulting high-resolution volume (HRV) obtained through the summation of the 22 LRVs. Note that the 22 virtual source lines were regularly spaced between the first and last emission source The figure also shows that each LRV has approximately constant amplitude along a trajectory in the $y'z$-plane. This is further demonstrated in Fig. 4, which highlights a trajectory with constant amplitude in a $y'z$-cross-section of the LRV. The trajectory depends on the virtual source position, and this is why it changes between the LRVs shown in Fig. 3. The trajectory from the different LRVs intersects at the point target, and the point can be resolved in 3-D, because the LRVs combine coherently at the intersection. The current RCA beamformer acquires each image point in the LRV independently, however by assuming the image values are sufficiently constant along the trajectories, the entire LRV can be obtained from a single $x'z$-cross-section of the LRV. The hypothesis is, thus, that it is only necessary to beamform one $x'z$-plane per emission to obtain the image points in the entire 3-D volume.

B. Second stage algorithm

The trajectory is the set of positions where the LRV image value is approximately constant. Such a trajectory can be obtained by solving for the set of image points, where the ToF is constant to the closest position of the aperture. The trajectory, $\vec{p}_t = (x_p, y', f(\vec{p}, y'))$, which intersect the image point $\vec{p}$, can, thus, be obtained by inserting $\vec{p}_t$ in (1) and solving for the trajectory's z-coordinate, yielding constant distance. This is achieved by solving for $f(\vec{p}, y')$ in the following equation:

$$d(\vec{p}_t, x_p) = d(\vec{p}, x_p). \tag{4}$$

This yields the following expression for the trajectory's z-position

$$f(\vec{p}, y') = \frac{d(\vec{p}, x_p)}{2} - \frac{(y_v - y')^2}{2d(\vec{p}, x_p) - 4z_v}. \tag{5}$$

Please refer to the supplementary materials for a detailed derivation of (5). Note that x_e in (1), in the above equations, has been substituted with x_p. This is because x_p is the image point's closest x'-position to the receiving aperture. This substitution is necessary, as there otherwise only exist solutions in very specific circumstances. The trajectory is, therefore, derived from a simplified ToF model, and consequently, the amplitude will change slightly as a function of the trajectory's z-coordinate. The solution obtained can be interpreted as the set of positions with constant ToF relative to the aperture's active part assuming dynamic receive apodization. This is why the image values are still close to constant along the trajectory.

Eq. (5) can for plane wave imaging be further simplified from the derivative and by placing the virtual source infinitely far away, yielding plane wave. This is because if the derivative is constant, then the trajectory is a straight line. The derivative of (5) is:

$$\frac{df(\vec{p}, y')}{dy'} = \frac{y_v - y'}{d(\vec{p}, x_p) - 2z_v}. \tag{6}$$

Substituting y_v and z_v in (6) with $r\sin(\phi)$ and $-r\cos(\phi)$ and letting $r \to \infty$ yield

$$\frac{df(\vec{p}, y')}{dy'} = \frac{\sin(\phi)}{1 + \cos(\phi)} = \tan(\phi/2). \tag{7}$$

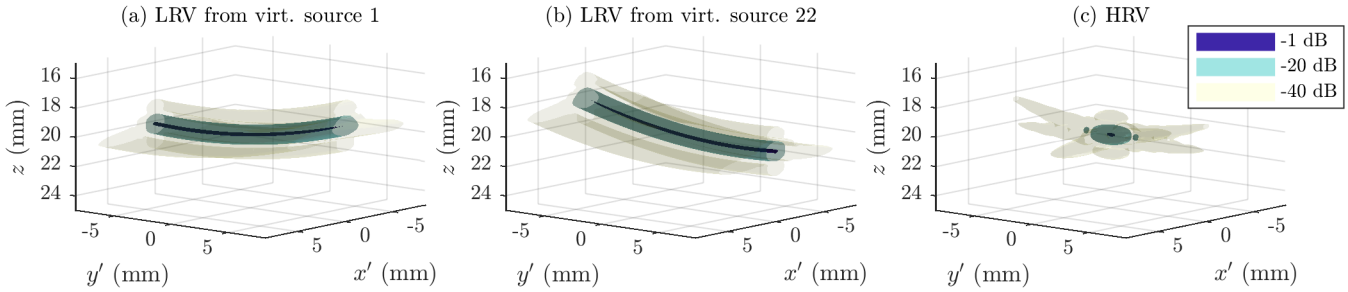

Fig. 3. 3-D surface representation of a point spread function (PSF) of a point target at $(x', y', z) = (0, 0, 20)$ mm. (a) shows the PSF in the LRV from the first emission, where the virtual line source position is $(x', y', z) = (x', -5.4, -5.4)$ mm. (b) shows the PSF in the LRV from the last (22nd) emission, where the virtual line source position is $(x', y', z) = (x', 5.4, -5.4)$ mm. (c) Shows the resulting HRV from combining the $N_e = 22$ LRVs from the emission sequence. Note that the 22 emissions were regularly spaced between the first (a) and last (b) emission.

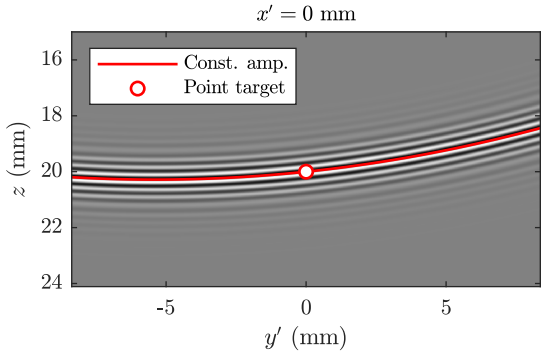

Fig. 4. LRV cross-section in linear scale space. The LRV corresponds to the 3-D LRV shown in Fig. 3a. The imaging scheme cannot resolve the point target from a single LRV, and there is an approximately constant value along curves across the cross-section. The curve intersecting the point target is colored red.

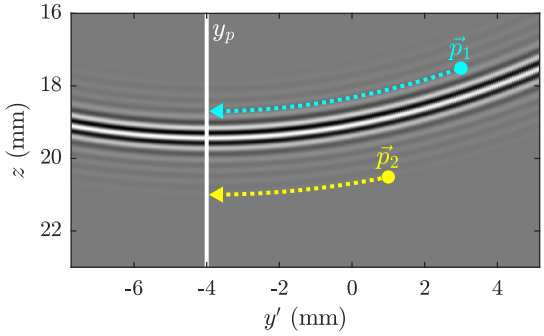

Fig. 5. Illustration of how two image points, $\vec{p}_1$ and $\vec{p}_2$, can be mapped onto the axial line, at $y' = y_p$ (white line), via the trajectories (dashed lines) defined by (5). The image value at $\vec{p}_1$ and $\vec{p}_2$ can subsequently be determined as the image values at the trajectories intersection with the axial line.

Here ϕ denotes the transmit angle. The equation states that the trajectory's slope is half of the slope of the transmitted plane wave. Therefore the trajectory's z-position for plane wave imaging can be simplified to

$$f_{plane}(\vec{p}, y') = z_p + \tan(\phi/2)(y' - y_p). \tag{8}$$

In Fig. 4 the trajectory plotted on top of the LRV cross-section is obtained by calculating $f(\vec{p}, y')$ with $\vec{p} = (0, 0, 20)$ mm. The figure shows that the image values are approximately constant along the curved trajectory and that the trajectory intersects $\vec{p} = (0, 0, 20)$ mm. It would, therefore, be redundant to beamform all the image points on the trajectory if, for instance, the image value at $\vec{p}$ was known.

Moreover, since any position on the 2-D cross-section can be mapped via their trajectory onto one axial line in the cross-section, it is only necessary to beamform a single axial line to obtain the entire 2-D LRV cross-section. Similarly, it is only necessary to beamform one 2-D plane in the LRV to obtain the entire 3-D LRV, since any 3-D position in the volume can be mapped onto a single $x'z$-plane. An example of this mapping is visualized in Fig. 5. The figure shows how two image points, $\vec{p}_1$ and $\vec{p}_2$, are, via their trajectories, mapped on to the axial line at $y' = y_p$. Note that the image values at $\vec{p}_1$ and $\vec{p}_2$ can be derived as the image value at the trajectories' intersections with the axial line. The function maps any position via its corresponding trajectory onto the $x'z$-plane at $y' = y_p$, and is given by

$$(x', y', z) \mapsto (x', y_p, f((x', y', z), y_p)), \tag{9}$$

where, $f((x', y', z), y_p)$, can be simplified to

$$f((x', y', z), y_p) = \begin{cases} z + \frac{(y'-y_p)(2y_v - y' - y_p)}{2\left(z_v - z + \sqrt{(y'-y_v)^2 + (z-z_v)^2}\right)} & \text{if } z < z_v \\ z + \frac{(y'-y_p)(2y_v - y' - y_p)}{2\left(z_v - z - \sqrt{(y'-y_v)^2 + (z-z_v)^2}\right)} & \text{otherwise.} \end{cases} \tag{10}$$

For plane wave imaging, the mapping equation can be obtained by substituting, $f((x', y', z), y_p)$, in (9), with

$$f_{plane}((x', y', z), y_p) = z + \tan(\phi/2)(y_p - y'). \tag{11}$$

Note that (10) is obtained by changing the input variables of (5), such that it yields the z-coordinate at $y' = y_p$ of the trajectory that intersects (x', y', z). Using (9), any LRV image value in the volume can be obtained by interpolating the image values on a beamformed xz'-plane at the mapped positions. Furthermore, since (10) and (11) are independent of x', it is only necessary to calculate the mapping for every unique (y', z)-coordinates. Therefore, assuming the volume is

beamformed in a 3-D grid of size $N_w \times N_w \times N_z$, it is only necessary to calculate the mapped positions $N_w N_z$ times per emission. In contrast, the conventional approach requires the ToF to be calculated $N N_w^2 N_z$ times per emission.

C. Operations per high-resolution volume

To summarize, the proposed RCA beamformer consists of two stages. The first stage beamforms the $x'z$-plane at $y' = y_p$ using the conventional RCA beamformer, and the second stage maps the remaining coordinates onto the plane and interpolates their image value. To beamform an $N_w \times N_w \times N_z$ HRV, the first stage thus uses $NSN_wN_zN_e$ operations, which is the number of operations required beamform one $x'z$-plane for each emission with the conventional beamformer. Here $S = f_{z,1}/f_{z,2}$, where $f_{z,1}$ is the first stage axial sampling frequency of the $x'z$-plane, and $f_{z,2}$ is the axial sampling frequency of the final output. Consistent with other sequential beamformation methods [26], [29], accurate second stage interpolation can be achieved with $f_{z,1} \approx 8\lambda^{-1}$, where λ denotes the wavelength of the emitted pulse. The imaging accuracy against $f_{z,1}$ is further investigated in Section IV-C. Lastly, the second stage uses $N_wN_wN_zN_e$ operations to obtain the final HRV output. This is the number of operations required to reconstruct $N_w \times N_w \times N_z$ HRV from the beamformed planes obtained during the first stage. The two stages thus combined requires $NSN_wN_zN_e + N_wN_wN_zN_e = (NS+N_w)N_wN_zN_e$ operations to the beamform the HRV, whereas the conventional beamformer would require $NN_w^2N_zN_e$ operations.

Consistent with other sequential beamformation methods [26], [29], accurate second stage interpolation can be achieved with $f_{z,1} \approx 8\lambda^{-1}$, where λ denotes the wavelength of the emitted pulse. The imaging accuracy against $f_{z,1}$ is further investigated in Section IV-C.

Table I compares the number of operations across different 3-D imaging methods. It is assumed that the beamformed rectangular volume contains $N_w^2 N_z = 128 \times 128 \times 1024$ image points, that the HRV was acquired with $N_e = 32$ emissions and that $S = 4$. Furthermore, the number of operations required to beamform an $N_w \times N_z$ image plane with an ordinary linear 1-D array is added for additional information. The table shows that the proposed 3-D imaging method brings the number of operations to the same order of magnitude as in ordinary 2-D imaging. In comparison, the conventional RCA imaging method requires two orders of magnitude more operations, and 3-D imaging with the fully populated 2-D array requires three to four orders of magnitude more operations. This suggests that the proposed method can achieve real-time 3-D imaging on hardware similar to current scanners.

TABLE I
NUMBER OF OPERATIONS ACROSS DIFFERENT IMAGING METHODS

3-D imaging method	Number of operations
Fully populated 2-D array $N = 128$	$N^2N_w^2N_zN_e = 8796.1 \times 10^9$
Fully populated 2-D array $N = 32$	$N^2N_w^2N_zN_e = 549.8 \times 10^9$
Row-column addressed array $N = 128$ (Conventional)	$NN_w^2N_zN_e = 68.7 \times 10^9$
Row-column addressed array $N = 128$ (Proposed)	$(NS + N_w)N_wN_zN_e = 2.7 \times 10^9$
2-D imaging method	**Number of operations**
Linear 1-D array $N = 128$	$NN_wN_zN_e = 0.5 \times 10^9$

$N_e = 32$, $N_w = 128$, $N_z = 1024$, $S = 4$

D. Placement of the beamformed $x'z$-plane

The beamformed $x'z$-plane's y'-position, i.e., y_p, can be chosen arbitrarily (see (9)). However, because the trajectory's amplitude will deviate slightly as a function of it's z-position, it is recommended to set y_p to equal the y'-position of the trajectory's mean z-position within the FoV.

For plane wave imaging, it is therefore recommended to place the $x'z$-plane at the center of the volume. Nevertheless, in this work, $y_p = y_v$ because this position slightly simplifies the mapping (see (10)) and because this position contains the highest weighted image plane of the LRV, due to the spatial apodization applied before the LRV summation (see Section II-E). Nevertheless, the impact of the $x'z$-plane's position is investigated further in the result section (See Section IV-C).

E. Apodization

RCA imaging can contain several layers of apodization, some of which are unique for the RCA probe. The different apodization methods include: transmit apodization, dynamic receive apodization, integrated roll-off apodization [10], and spatial apodization, which has also been referred to as dynamic transmit apodization [22]. This section will elaborate on the last two methods of apodization as they are less known.

The purpose of integrated roll-off apodization is to reduce the edge waves produced at the line element's ends. This is done because edge waves cause the point spread function (PSF) to appear repeated along the axial direction erroneously. These repeats' are in [10] referred to as ghost echoes, and their largest signal strength is typically -20 dB lower than the main signal. The ghost echoes' amplitude can, however, be reduced outside the 60 dB dynamic range by tapering off the signal strength towards the ends of each line element. Note that integrated roll-off apodization cannot be applied through post-processing and must be directly built into the probe. The Vermon $128+128$ RCA-probe used in this work does not have integrated roll-off apodization. However, roll-off apodization was added to the simulated version of the probe. Here the added length of the roll-off region [10] was 15 element pitch, and the function used to taper off the edges correspond to the Hann function. As such, the simulation results, in Section IV, are from a more idealized version of the probe.

The spatial apodization is a weight applied to each image point of the LRV based on the point's distance from the transmitted beam's center. This can be done to more accurately model each LRV's spatial contribution to the final HRV and can be used to reduce side-lobe levels along the y'-direction.

TABLE II
B-MODE ACQUISITION PARAMETERS

Parameter	Value	Unit
No. elements	$128 + 128$	
Center frequency	6	MHz
Cycles in transmit pulse	2	
Speed of sound	1540	m/s
Element pitch	0.27	mm
Emissions per image	192†, 48‡	
Transmit/receive apodization	von Hann	
No. active elements in transmit	32	
Transmit/receive F-number	-1/1	
Channel sampling frequency	31.25	MHz
1st stage axial sampling frequency	8	λ^{-1}

†Fig. 6-9, Fig. 11-13 & Video 1
‡Table III & Video 2-6

In this work, the LRV image values are Hann weighted by the following equation

$$w(y', z) = \begin{cases} \cos^2\left(\frac{\pi|F\#(y'-y_v)|}{|z'-z_v|}\right) & \text{if } \frac{|F\#(y'-y_v)|}{|z'-z_v|} < \frac{1}{2} \\ 0 & \text{otherwise} \end{cases}, \tag{12}$$

where $F\#$ denotes the transmit F-number. The LRVs' image points are thus multiplied by their corresponding $w(y', z)$-value before the LRVs are summed to form the HRV.

III. Evaluation setup

The performance was primarily evaluated through cyst phantom measurements, in-vivo Sprague-Dawley rat kidney measurements, and Field II simulations of point targets. Here the cyst phantom (Dansk Fantom Service, Model 571) consists of a tissue-mimicking material with an attenuation of $0.5\,\mathrm{dB}/(\mathrm{MHz} \times \mathrm{cm})$. Additional measurements were performed to acquire 3-D B-mode videos processed using the proposed beamformer. These videos show the acquisition of moving particles in water and tissue motion in a carotid artery phantom during multiple pump cycles. See [41] for a detailed description of the carotid artery phantom setup.

The measurements were performed with a Vermon $128{+}128$ RCA probe connected to a Verasonics Vantage 256 research scanner, and the simulations used the same transducer and sequence parameters. See Table II for a parameter overview. The imaging sequence used 96 row emissions and 96 column emissions, transmitted with a sliding aperture of 32 elements apodized with a Hann window. However, a shorter sequence of 48 row emissions was also used when acquiring most of the B-mode videos found in the supplementary materials. The transmit and receive F-number was set to -1 and 1, and the RF data was acquired with a sampling rate of 31.25 MHz. Also, unless stated otherwise, the first stage beamformation of the $x'z$-plane was performed at $y_p = y_v$ (see Section II) and at an axial sampling rate of $f_{z,1} = 8\lambda^{-1}$. Lastly, the second stage beamformation was performed using spline interpolation.

A. Image similarity

The output similarity of the two beamformation methods was determined from visual inspection of B-mode images, the full width at half maximum (FWHM), the full width at tenth maximum (FWTM), and by the relative absolute error (RAE) given by

$$\mathrm{RAE} = \frac{\sum_{i=1}^{K} |X_i - Y_i|}{\sum_{i=1}^{K} |Y_i - \bar{Y}|}. \tag{13}$$

Here X and Y are the B-mode output, containing K image points, from respectively the proposed and conventional beamformer and $\bar{Y}$ denote the mean image value of Y.

The RAE value was used to determine the appropriate axial sampling of the $x'z$-plane for accurate second stage interpolation. This sampling rate was determined as the axial sampling rate by which the RAE value converges.

The image quality was determined through the FWHM and FWTM along the axial and lateral directions. The FWHM and FWTM are calculated as the PSF's width at -6 dB and -20 dB in the axial and lateral directions, and the PSFs were simulated using Field II.

B. Phase similarity

The phase shift between the conventional and proposed methods' output was estimated to determine whether the phase information was preserved. It should be noted that slight phase shifts between the two methods can be tolerated. It is more important that the phase shifts between the proposed method's consecutive HRVs are correct. To demonstrate this, flow profiles obtained with the conventional and proposed beamformer are presented. The acquisition of stationary parabolic flow in a 6 mm radius tube was simulated using Field II by moving uniformly distributed point targets along the flow field. The simulation was performed with a peak velocity of 25 cm/s and a beam-to-flow angle of $75°$. See [38] for additional details regarding the parabolic flow simulation.

The applied flow acquisition sequence was identical to the sequence used in [41]. This sequence contains 32 unique emission sources, transmitted from the Vermon RCA probe with a center frequency of 3 MHz at $f_{prf} = 10$ kHz.

The axial velocity profiles were estimated using the auto-correlation estimator [42], and the profiles were obtained from the axial line, which intersects the simulated tube's center. The estimation accuracy was determined by the relative absolute bias (RB), i.e., the mean absolute difference between the estimated average profile and the actual profile. The precision was determined as the relative mean standard deviation over the profile (RSD). Both the bias and standard deviation were normalized to the peak velocity. These statistics were derived from 134 profile estimates, and each estimate was obtained with an ensemble length corresponding to 32 HRVs.

C. Processing time

The processing time of both beamformation methods was evaluated by plotting the LRV beamformation time against increasing values of $L = N_w = N$. This means that the number of channels and samples in the beamformed volume's

width were increased simultaneously in the analysis. Also, it is assumed that $S = 4$ and $N_z = 512$.

The conventional RCA beamformation was performed using the CUDA C/C++ implementation of the RCA beamformer presented in [22], and the second stage beamformation was performed, with GPU (graphical processing unit) acceleration, using MATLAB's (MathWorks Inc., version R2022b) built-in interpolation function, `interp1`. The interpolation method used for the RCA beamformer was a cubic interpolation, and the second stage beamformer was, as previously mentioned, implemented with spline interpolation. Furthermore, the input RF channel was in the comparative analysis, complex with the dimensions of $1218 \times L$. Lastly, the built-in function, `gputimeit`, was used to derive the processing time.

The processing time was also evaluated on measured data. Here the timed results were derived from the processing time of beamforming 500 HRVs, which was estimated using the `tic` and `toc` functions. The measured results demonstrate the performance in three different beamformation scenarios. The first is the beamformation of a $20 \times 20 \times 60$ mm^3 volume covered by $100 \times 100 \times 250$ image points. Here the RF channel data has the dimension of 2302×128 and $S = 8$. In the second scenario, a smaller $20 \times 20 \times 30$ mm^3 volume covered by $100 \times 100 \times 125$ image points is beamformed. Here the RF channel data has the dimensions 1278×128 and $S = 8$. In the last scenario, a $20 \times 20 \times 15$ mm^3 volume is covered by $100 \times 100 \times 200$ image points. Here the RF signal has the dimensions of 671×128 and $S = 2$. The latter scenario emulates the often dense sampling used in functional imaging. In contrast, the former two demonstrate the processing time for a large and mid-sized B-mode volume beamformed with roughly λ axial spacing between the image points. Videos of the resulting beamformed volumes are included in the supplementary materials.

The volumes were, in all cases, beamformed from complex, single-precision floating point numbers, and the beamformation includes dynamic receive apodization and the spatial apodization described in Section II-E. Matched filtration was, however, not included when timing the beamformation.

Lastly, both methods were timed on a computer with an NVIDIA GeForce RTX 3090 graphics card and a 3 GHz Intel Xeon Gold 6136 central processing unit.

IV. Results

A. Image quality comparison

Fig. 6-8 compares the B-modes images obtained with the conventional and proposed beamformer. Fig. 6 compares the 2-D B-mode images of a rat kidney, and Fig. 7 and 8 compare the 2-D and 3-D B-mode image of a cyst phantom. The supplemental materials also include a video of the 3-D B-mode images shown in Fig. 8 rotating (See Video 1). The B-mode images and cyst phantom video show that the two beamformers achieve a visually indistinguishable result.

Fig. 9 show the beamformers' axial and lateral FWHM and FWTM at various depths. The lateral FWHM (FWHMx and FWHMy) was 0.27% to 0.62% larger when using the proposed approach. The most significant increase was found near the aperture, and at $z = 50$ mm, the relative increase converges towards approximately 0.30%. A similar trend can also be seen for the lateral FWTM (FWTMx and FWTMy), which was found to be 0.21% to 1.19% larger when using the proposed approach. The proposed method's increase to the axial FWHM (FWHMz) and FWTM (FWTMz) was relatively constant against the various depths, and the axial widths were found to be 0.20% to 0.50% and 0.36% to 0.37% larger with the proposed approach.

B. Phase similarity and velocity estimation

Fig. 7e-f shows the amplitude and phase change between the output of the conventional and proposed beamformer. Note that Fig. 7e shows the amplitude change in decibels (dB) relative to the maximum amplitude. The amplitude change across the entire 2-D output (See Fig. 7a-b) is on average -56.91 ± 4.69 dB, and the phase shift is on average 0.01 ± 0.04 radian.

Fig. 10 shows the velocity profile of simulated parabolic flow (see Section III-B), estimated with the conventional and proposed beamformer. The two profiles are visually identical, and Fig. 10c shows the profiles' maximum difference is less than 0.15 mm/s. Furthermore, the average standard deviation (RSD) is the same at two decimal places, and the difference in relative absolute bias (RB) is 0.02%.

C. First stage parameters: axial sampling rate and placement of the beamformed $x'z$-plane

Fig. 11 compares the proposed beamformer's output for different values of y_p, i.e., the y'-position of the $x'z$-plane beamformed during the first stage (see (9)). The output image is of randomly spaced point-targets, and Fig. 11a-d shows the output with $y_p = 0$ mm, $y_p = 5$ mm, $y_p = 10$ mm and $y_p = y_v$. Note that the latter configuration is used for the B-mode images presented in this paper.

Fig. 12a-c shows the proposed beamformer's simulated PSF at $z = 26$ mm against different axial sampling rates during the first stage beamformation ($f_{z,1}$). The figure shows that the side lobes levels in the proposed beamformer's output gradually reduce as the sampling rate increases. At the sampling rate of $f_{z,1} = 8\lambda^{-1}$, the PSF becomes indistinguishable from the conventional beamformer's PSF shown in Fig. 12d.

Fig. 13 plots the RAE value (see (13)) against increasing values of $f_{z,1}$. Here the RAE values was calculated from outputs of the 2-D cyst phantom image (See Fig. 7) and the simulated PSF at 26 mm (See Fig. 12). The plot shows the RAE values decrease towards zero and converges at about $f_{z,1} = 6\lambda^{-1}$ for the cyst phantom measurement and about $f_{z,1} = 7\lambda^{-1}$ for the simulated PSF. Note that the values are shown on a logarithmic scale.

D. Processing time

Fig. 14 shows the computation time for beamforming an $L \times L \times 512$ LRV acquired using an RCA probe with L receive channels. The computation time is plotted against increasing values of L, so both the number of image lines and channels are increased simultaneously.

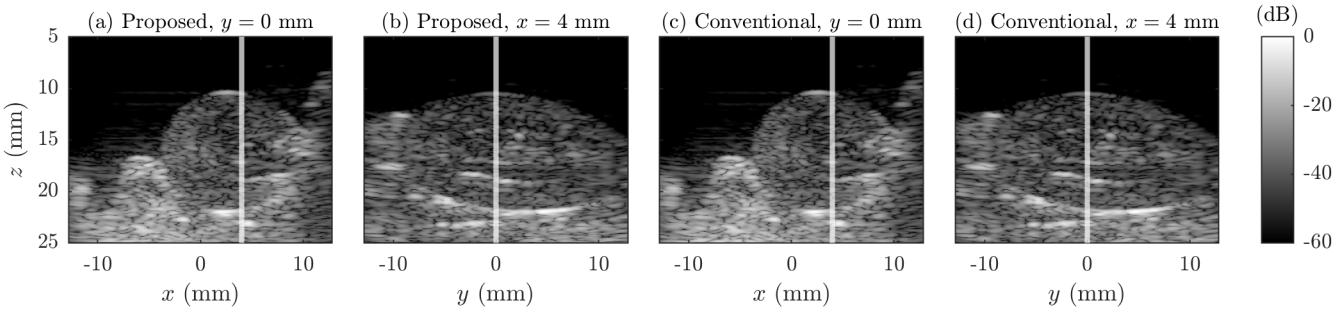

Fig. 6. In-vivo B-mode images of a Sprague-Dawley rat kidney beamformed with the proposed (a)-(b) and conventional (c)-(d) method. The kidney is shown in two cross-sections, and the white line indicates their relative position.

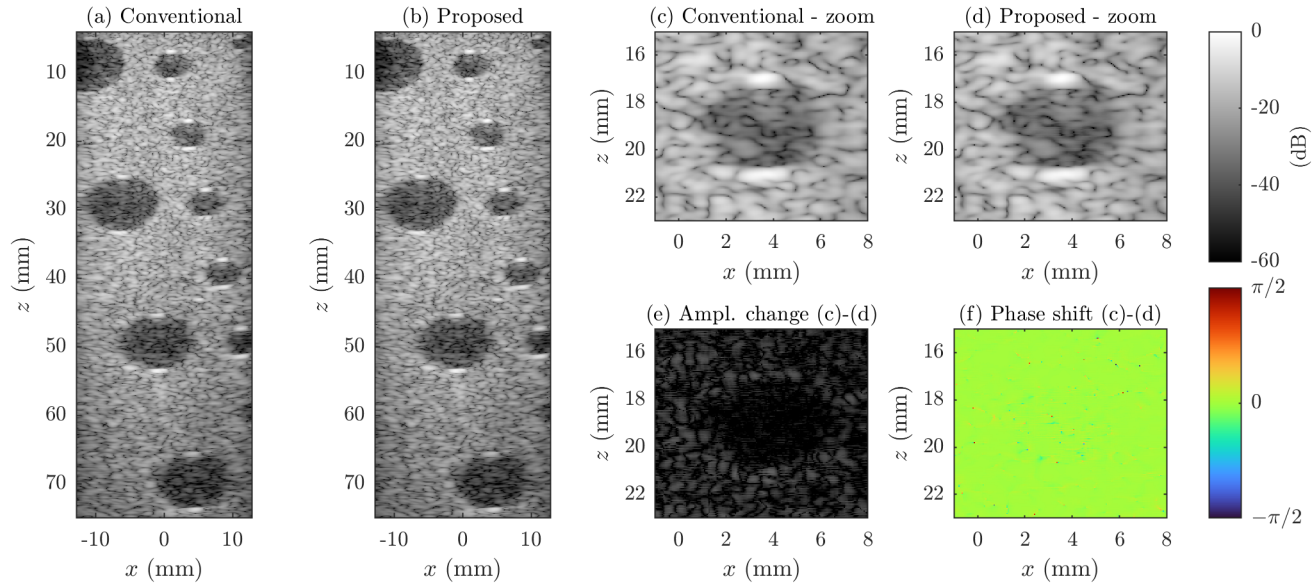

Fig. 7. Output comparison between the conventional DAS RCA beamformer (a) and the proposed beamformer (b). The beamformed image shows a 2-D slice of a cyst phantom designed for 3-D imaging. A 3-D rendering of the entire beamformed volume is shown in Fig. 8.

As the variable L increases, the computation time of the conventional RCA beamformer diverges from the computation time of the proposed RCA beamformer. For example, at $L = 64$, the computation time of the prior approach is 1.42 ms, whereas the new method achieves the beamformation in 0.52 ms. At $L = 512$, the computation time from the conventional approach is 539.21 ms, whereas the new method performs the beamformation in 12.03 ms.

Table III summarizes the measured timed results. The table shows the proposed method's volume frame rate for different volume sizes and the relative frame rate increase when compared to the conventional approach. The table also shows an estimate of the maximum pulse repetition frequency (f_{prf}) for real-time beamformation, which is derived as the volume frame rate times the number of emissions per volume.

V. Discussion

It has been demonstrated that the proposed beamformer achieves a virtually identical output to that of the conventional RCA beamformer, with much fewer operations. This was demonstrated both for B-mode imaging and when performing velocity estimation. The proposed beamformer only slightly impacted the image quality, and the increase to FWHM and FWTM was, for the majority of the cases, found to be below 1% (see Fig. 9). This can be considered a negligible increase, and visually it is practically impossible to distinguish between the outputs from the conventional and proposed beamformers. Similarly, differences between the flow profiles obtained from the conventional and proposed method were negligible. On average, the most significant estimation difference was less than 0.15 mm/s which is low considering the flow was simulated with a peak velocity of 25 cm/s.

The reduction in the number of operations translates to much faster processing times. For instance, the beamformation of an $L \times L \times 512$ volume with $N = L$ receiving channels was at $L = 512$ performed 44.8 times faster than the conventional method (see Fig. 14). However, despite the significant frame rate increase, it is still less than half of the theoretical increase of $NN_w/(NS + N_w) = L/(S + 1) = 102.4$ for $L = 512$ and $S = 4$. One reason for this discrepancy is that the theoretical

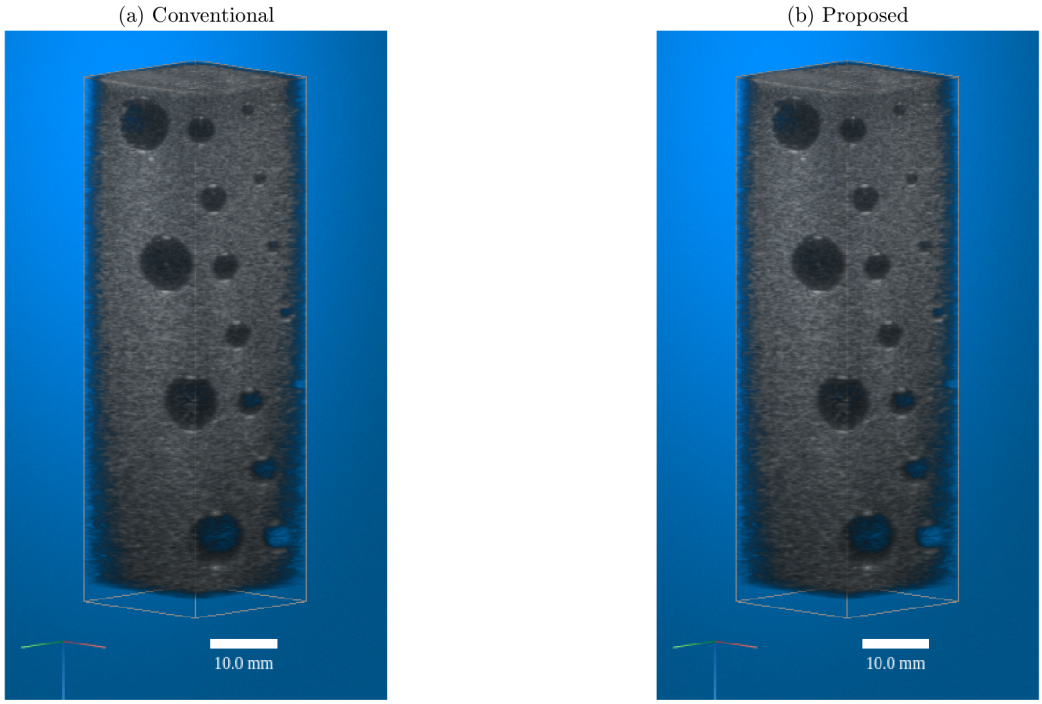

Fig. 8. 3-D rendering of the cyst phantom beamformed with the conventional DAS RCA beamformer (a) and the proposed beamformer (b). The volume is shown in a 60 dB dynamic range, and the scale bars show 10 mm relative to the volume. Note that a video of the 3-D rendering is included in the supplemental materials (see Video 1).

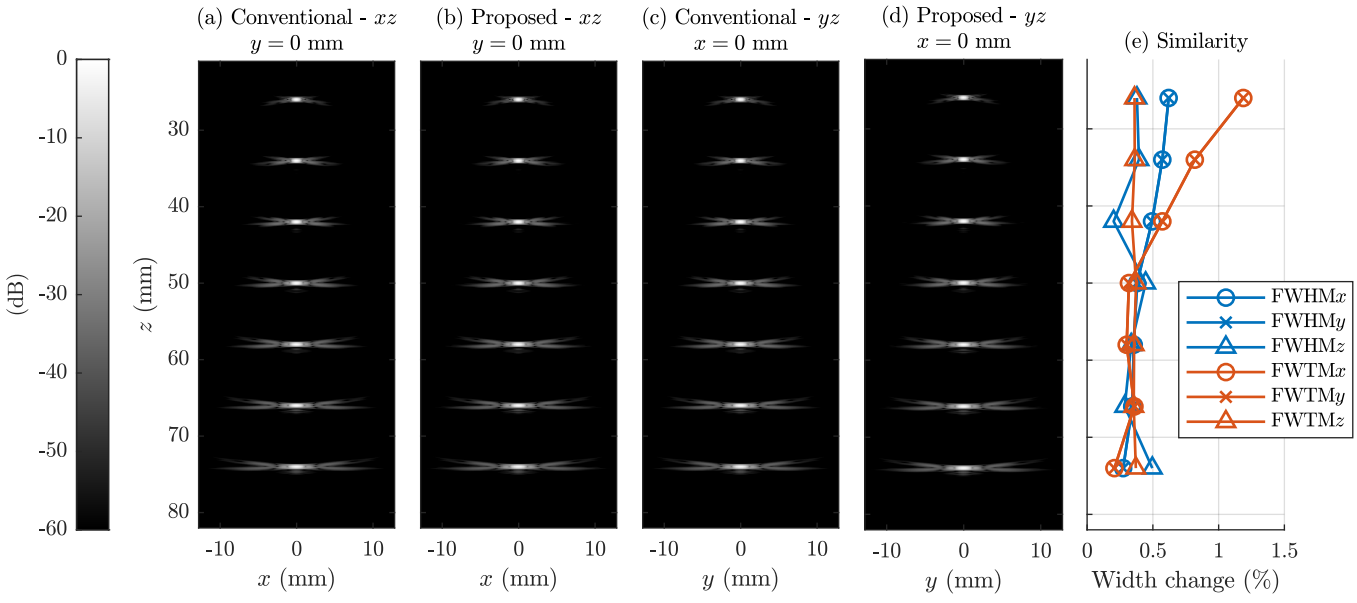

Fig. 9. PSFs from simulations of point targets. (a) and (c) show output obtained using the RCA DAS beamformer and (b) and (d) show the outputs obtained using the proposed beamformer. (e) plots the proposed beamformer's relative change in FWHM and FWTM along the x-, y- and z-direction. Note that (a)-(e) share the same vertical axis.

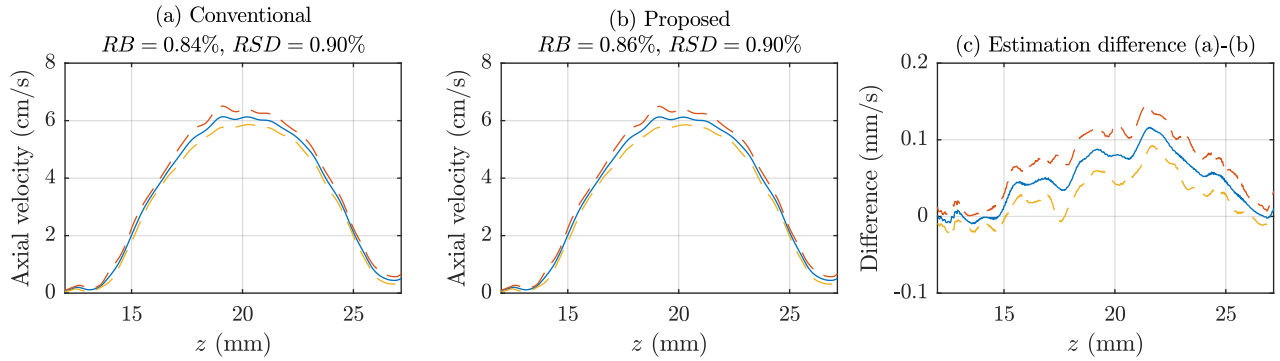

Fig. 10. Axial velocity profile of simulated flow obtained with the conventional (a) and proposed (b) beamformer. The estimation difference along z is shown in (c). Blue-line: average profile. Dashed lines: $\pm$ one standard deviation. The relative absolute bias (RB) and relative average standard deviation (RSD) are written above the corresponding profile.

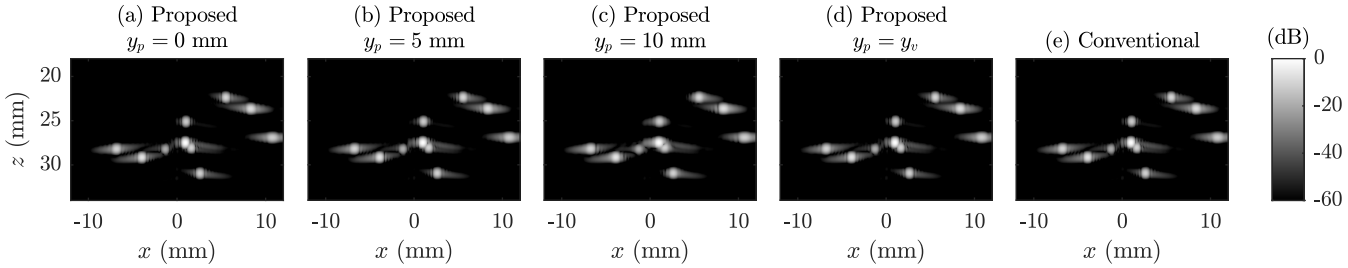

Fig. 11. B-mode images of randomly spaced simulated point targets. (a)-(d) show the output of the proposed beamformer with different y_p-values (see (9)), i.e. the y'-position of the beamformed $x'z$-plane during the first stage. For reference, (e) shows the output of the conventional beamformer.

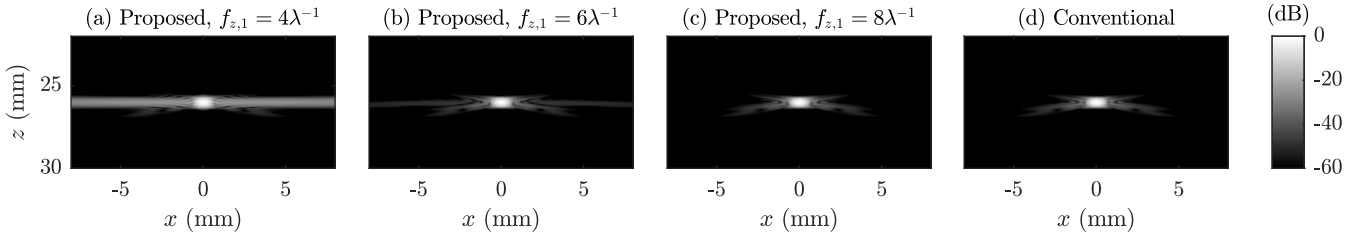

Fig. 12. Simulated PSFs obtained with various axial sampling rates during the first stage beamformation ($f_{z,1}$). The figure shows that the higher the sampling rate is during the first stage, the closer the output from the proposed beamformation resembles the RCA DAS beamformation output (d). The sidelobe levels are reduced each time $f_{z,1}$ is increased. (a) At $f_{z,1} = 4\lambda^{-1}$, the erroneous side lobe levels are around -26 dB. (b) At $f_{z,1} = 6\lambda^{-1}$ the sidelobe levels are below -48 dB. (c) At $f_{z,1} = 8\lambda^{-1}$, the output from the proposed beamformer is visually indistinguishable from the conventional beamformer's output (d).

TABLE III
MEASURED PROCESSING RATES

Channel data size	Volume size	Volume frame rate	Max f_{prf}	Frame rate increase	Output sparsity	Video
1278×128	$100 \times 100 \times 125$	21.31 Hz	1022.99 Hz	$\times 6.25$	$S = 8$	Video 2 & 3
2302×128	$100 \times 100 \times 250$	13.20 Hz	633.37 Hz	$\times 7.25$	$S = 8$	Video 4
671×128	$100 \times 100 \times 200$	37.60 Hz	1804.80 Hz	$\times 9.23$	$S = 2$	Video 5 & 6

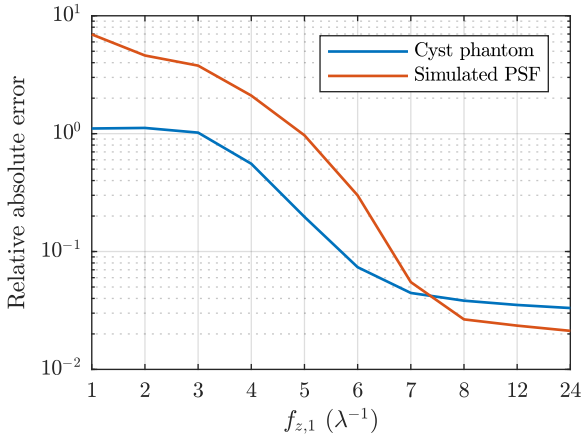

Fig. 13. Proposed beamformer's relative absolute error (RAE) against the axial sampling rate ($f_{z,1}$) used during the first stage beamformation. The RAE values are calculated from the simulated PSF at $(x, y, z) = (0, 0, 26)$ mm (See Fig. 12) and from the 2-D cross-section of the cyst phantom (See Fig 7).

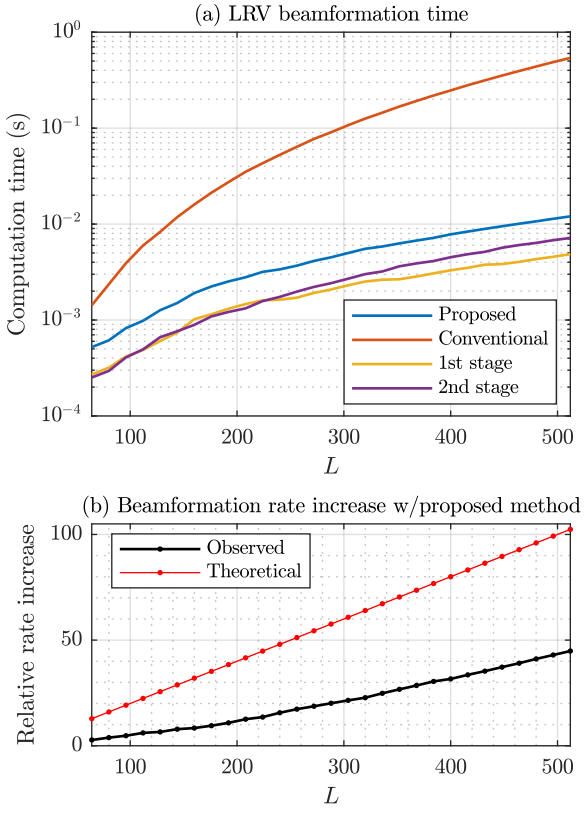

Fig. 14. The beamformers' computation time for beamforming an $L \times L \times 512$ LRV with L receiving channels. The top figure (a) plots the processing time against L, and the bottom figure (b) plots the proposed method's observed and theoretical increase in beamformation rate. Here the theoretical increase (red dotted line) is the reduction factor in number of operations, which equals $L/(S+1)$. Note that these results were obtained with $S = 4$ (see Section II-C). The red and blue line (a) plots the computation time of the conventional and proposed beamformer. The yellow and purple line plots the computation time of the two stages of the proposed beamformer. The proposed beamformer's computation time (blue line) is obtained by summing the computation time of the first and second stages.

increase assumes that the interpolation method is consistent throughout the beamformation. This is not the case because the second stage beamformation uses spline interpolation, whereas the conventional beamformer uses cubic interpolation. Changing the algorithm's interpolation method to cubic interpolation increases the proposed method's beamformation rate by $21.74 \pm 1.96\%$, which is not enough to reach the theoretical beamforming rate increase shown in Fig. 14b Another reason for the discrepancy is that the proposed beamformer is less efficiently implemented when compared to the conventional beamformer gauged against [22]. Note that the second stage solely consists of MATLAB's built-in functions, whereas the conventional beamformer is a much more carefully optimized CUDA C++ implementation. However, the primary purpose of this paper is to introduce the method, and optimization is left for future work.

The presented implementation of the proposed method was also found to be significantly faster on the measured data acquired with the Vermon RCA probe (see Table III). Here the proposed method increased the frame rate with a factor ranging from 6.25 to 9.23 between the different beamformation scenarios. The scenario with the highest frame was the latter, where a $100 \times 100 \times 200$ high-resolution volume is beamformed at a volume frame rate of 37.60 Hz. Here, real-time beamformation is achieved with an $f_{prf} \leq N_e \times 37.60\,\text{Hz} = 1804.80\,\text{Hz}$. This scenario was found to be fastest to beamform first and foremost because $S = 2$, whereas $S = 8$ in the other scenarios, but also because the size of RF channel data was the smallest. Note that the smaller input size is also why this scenario yields the highest volume frame rate with the conventional beamformer, despite the high-resolution volume being the second largest of the three scenarios investigated.

Fig. 11 and 12 demonstrate the impact of the imaging parameters used in first stage beamformation. Fig. 11 shows the impact of the beamformed $x'z$-plane's y'-position, i.e. y_p (see (10)). When the plane is fixed at the center, i.e., when $y_p = 0$ mm (see Fig. 11a), or when the plane follows the emission source, i.e., when $y_p = y_v$ (see Fig. 11d), the output becomes indistinguishable from the conventional method's output (see Fig. 11e). When the plane is fixed off center (see Fig. 11b-c), the PSFs get slightly wider, especially when $y_p = 10$ mm (notice, e.g., the point-target at the center of the B-mode image). This is due to the amplitude changing slightly along the trajectory (see (5)). When using dynamic receive apodization, the highest amplitude will most likely be at the trajectory's largest z-position because, here, most elements are active during receive. Similarly, the lowest amplitude will most likely be at the trajectory's minimum z-position. To account for this change in amplitude, one could scale the amplitude of the reconstructed LRV relative to the corresponding trajectory's peak or valley point. This can, e.g., be done by applying the following amplitude scaling factor

$$W(x', y', z) = \frac{z}{f((x', y', z), y_v)}, \tag{14}$$

on each LRV before summation. This scaling factor accounts for the change in aperture width along trajectory when using dynamic receive apodization. However, in practice, the

impact of the amplitude change is very subtle, making it somewhat unnecessary to apply additional image scaling, at least with the suggested $y_p = y_v$ configuration.

Fig. 12 and 13 show the impact of the beamformed $x'z$-plane axial sampling rate, i.e. $f_{z,1}$. Fig. 12 confirm visually that the axial sampling should be $f_{z,1} \approx 8\lambda^{-1}$ for accurate interpolation, and Fig. 13 shows that output difference between conventional and proposed method converges at around $f_{z,1} \approx 8\lambda^{-1}$, if not lower sampling rate for the cyst phantom measurement. This suggests S should be fixed to equal $S = f_{z,1}/f_{z,2} = 8/(\lambda f_{z,2})$ for accurate second stage reconstruction.

Future work will investigate the viability of the proposed beamformer for more complex functional imaging methods such as 3-D power Doppler, vector flow imaging, and super-resolution imaging. In addition, effective visualization of the 3-D data should also be investigated, as 3-D structures can, depending on the presentation, be challenging to apprehend.

VI. Conclusion

An RCA beamformer was developed, which significantly reducing the computation time and allowing for real-time volumetric beamformation on the Verasonics Vantage System when employing an NVIDIA GeForce RTX 3090 graphics card. The proposed beamformer was demonstrated to be capable of beamforming an LRV consisting of $L^2 N_z = 512^3$ complex samples from data acquired with an RCA with $L = 512$ channels in receive in 12.03 ms, about 45 times faster than the conventional beamformer. Furthermore, from measured data acquired using the 128+128 Vermon RCA probe, the proposed beamformer could beamform a $100 \times 100 \times 200$ sized volume at a volume frame rate of 37.60 Hz, which was more than nine times faster than the conventional approach.

The proposed beamformer yields an output visually indistinguishable from the conventional approach, and the relative change in axial and lateral FWHM/FWTH was, in most cases, below 1%. This demonstrates that the delay simplifications used to derive the proposed method have a negligible impact on the image quality.

VII. Acknowledgement

We thank Nathalie Sarup Panduro, Sofie Bech Andersen and Charlotte Mehlin Sørensen (Department of Biomedical Sciences, University of Copenhagen, DK-2200, Copenhagen, Denmark) for providing the experimental setup for the Sprawley rat kidney measurement and for performing the acquisition.

This work involved animals in its research. Approval of all ethical and experimental procedures and protocols was granted by the Danish Animal Experiments Inspectorate under the Ministry of Environment and Food under Application No. 2020-15-0201-00547.

This work was financially supported by European Research Council's (ERC) Synergy Grant 854796.

References

[1] S. W. Smith, H. G. Pavy, and O. T. von Ramm, "High speed ultrasound volumetric imaging system – Part I: Transducer design and beam steering," *IEEE Trans. Ultrason. Ferroelec. Freq. Contr.*, vol. 38, pp. 100–108, 1991.

[2] O. T. von Ramm, S. W. Smith, and H. G. Pavy, "High speed ultrasound volumetric imaging system – Part II: Parallel processing and image display," *IEEE Trans. Ultrason. Ferroelec. Freq. Contr.*, vol. 38, pp. 109–115, 1991.

[3] A. Austeng and S. Holm, "Sparse 2-D arrays for 3-D phased array imaging - design methods," *IEEE Trans. Ultrason. Ferroelec. Freq. Contr.*, vol. 49, pp. 1073–1086, August 2002.

[4] C. E. Morton and G. R. Lockwood, "Theoretical assessment of a crossed electrode 2-D array for 3-D imaging," in *Proc. IEEE Ultrason. Symp.*, pp. 968–971, 2003.

[5] S. I. Awad and J. T. Yen, "3-D spatial compounding using a row-column array," *Ultrason. Imaging*, vol. 31, no. 2, pp. 120–130, 2009.

[6] C. H. Seo and J. T. Yen, "A 256 x 256 2-D array transducer with row-column addressing for 3-D rectilinear imaging," *IEEE Trans. Ultrason. Ferroelec. Freq. Contr.*, vol. 56, pp. 837–847, April 2009.

[7] A. Sampaleanu, P. Zhang, A. Kshirsagar, W. Moussa, and R. Zemp, "Top-orthogonal-to-bottom-electrode (TOBE) CMUT arrays for 3-D ultrasound imaging.," *IEEE Trans. Ultrason. Ferroelec. Freq. Contr.*, vol. 61, no. 2, pp. 266–276, 2014.

[8] C. E. M. Démoré, A. W. Joyce, K. Wall, and G. R. Lockwood, "Real-time volume imaging using a crossed electrode array," *IEEE Trans. Ultrason., Ferroelec., Freq. Contr.*, vol. 56, no. 6, pp. 1252–1261, 2009.

[9] A. W. Joyce and G. R. Lockwood, "Crossed-array transducer for real-time 3D imaging," in *Proc. IEEE Ultrason. Symp.*, pp. 2116–2120, 2014.

[10] M. F. Rasmussen, T. L. Christiansen, E. V. Thomsen, and J. A. Jensen, "3-D imaging using row–column-addressed arrays with integrated apodization — Part I: Apodization design and line element beamforming," *IEEE Trans. Ultrason. Ferroelec. Freq. Contr.*, vol. 62, no. 5, pp. 947–958, 2015.

[11] J. A. Jensen, M. Schou, L. T. Jørgensen, B. G. Tomov, M. B. Stuart, M. S. Traberg, I. Taghavi, S. H. Øygaard, M. L. Ommen, K. Steenberg, and et. al., "Anatomic and functional imaging using row-column arrays," *IEEE Trans. Ultrason. Ferroelec. Freq. Contr.*, vol. 69, pp. 2722–2738, October 2022.

[12] R. E. Davidsen, J. A. Jensen, and S. W. Smith, "Two-dimensional random arrays for real time volumetric imaging," *Ultrason. Imaging*, vol. 16, pp. 143–163, July 1994.

[13] S. S. Brunke and G. R. Lockwood, "Broad-bandwidth radiation patterns of sparse two-dimensional vernier arrays," *IEEE Trans. Ultrason. Ferroelec. Freq. Contr.*, vol. 44, pp. 1101–1109, sep 1997.

[14] J. T. Yen and S. W. Smith, "Real-time rectilinear volumetric imaging using a periodic array," *Ultrasound in Medicine & Biology*, vol. 28, pp. 923–931, jul 2002.

[15] A. Austeng and S. Holm, "Sparse 2-D arrays for 3-D phased array imaging - Design methods," *IEEE Trans. Ultrason. Ferroelec. Freq. Contr.*, vol. 49, no. 8, pp. 1073–1086, 2002.

[16] B. Diarra, M. Robini, P. Tortoli, C. Cachard, and H. Liebgott, "Design of optimal 2-D nongrid sparse arrays for medical ultrasound," *IEEE Trans. Biomed. Eng.*, vol. 60, no. 11, pp. 3093–3102, 2013.

[17] A. Ramalli, E. Boni, E. Roux, H. Liebgott, and P. Tortoli, "Design, implementation, and medical applications of 2-D ultrasound sparse arrays," *IEEE Trans. Ultrason. Ferroelec. Freq. Contr.*, pp. 1–1, 2022.

[18] J. D. Larson, III, "2-D phased array ultrasound imaging system with distributed phasing." Patent US 5229933, July 1993.

[19] B. Savord and R. Solomon, "Fully sampled matrix transducer for real time 3D ultrasonic imaging," in *Proc. IEEE Ultrason. Symp.*, vol. 1, pp. 945–953, 2003.

[20] S. Blaak, Z. Yu, G. C. M. Meijer, C. Prins, C. T. Lancee, J. G. Bosch, and N. de Jong, "Design of a micro-beamformer for a 2D piezoelectric ultrasound transducer," in *Proc. IEEE Ultrason. Symp.*, pp. 1338–1341, sep 2009.

[21] P. Santos, G. U. Haugen, L. Løvstakken, E. Samset, and J. D'hooge, "Diverging wave volumetric imaging using subaperture beamforming," *IEEE Trans. Ultrason. Ferroelec. Freq. Contr.*, vol. 63, no. 12, pp. 2114–2124, 2016.

[22] M. B. Stuart, P. M. Jensen, J. T. R. Olsen, A. B. Kristensen, M. Schou, B. Dammann, H. H. B. Sørensen, and J. A. Jensen, "Real-time volumetric synthetic aperture software beamforming of row-column probe data," *IEEE Trans. Ultrason. Ferroelec. Freq. Contr.*, vol. 68, no. 8, pp. 2608–2618, 2021.

[23] L. T. Jørgensen, M. S. Traberg, M. B. Stuart, and J. A. Jensen, "Performance assessment of row-column transverse oscillation tensor velocity imaging using computational fluid dynamics simulation of carotid bifurcation flow," *IEEE Trans. Ultrason. Ferroelec. Freq. Contr.*, vol. 69, no. 4, pp. 1230–1242, 2022.

[24] V. Hingot, C. Errico, B. Heiles, L. Rahal, M. Tanter, and O. Couture, "Microvascular flow dictates the compromise between spatial resolution

and acquisition time in ultrasound localization microscopy," *Scientific Reports*, vol. 9, no. 1, pp. 1–10, 2019.
[25] D. E. Knuth, "Big omicron and big omega and big theta," *SIGACT News*, vol. 8, no. 2, pp. 18–24, 1976.
[26] J. Kortbek, J. A. Jensen, and K. L. Gammelmark, "Sequential beamforming for synthetic aperture imaging," *Ultrasonics*, vol. 53, no. 1, pp. 1–16, 2013.
[27] T. Di Ianni, C. Villagomez-Hoyos, C. Ewertsen, T. Kjeldsen, J. Mosegaard, and J. A. Jensen, "A vector flow imaging method for portable ultrasound using synthetic aperture sequential beamforming," *IEEE Trans. Ultrason. Ferroelec. Freq. Contr.*, vol. 64, no. 11, pp. 1655–1665, 2017.
[28] M. C. Hemmsen, P. M. Hansen, T. Lange, J. M. Hansen, K. L. Hansen, M. B. Nielsen, and J. A. Jensen, "In vivo evaluation of synthetic aperture sequential beamforming," *Ultrasound Med. Biol.*, vol. 38, no. 4, pp. 708–716, 2012.
[29] H. Vos, P. van Neer, M. M. Mota, M. Verweij, A. van der Steen, and A. Volker, "F-k domain imaging for synthetic aperture sequential beamforming," *IEEE Trans. Ultrason. Ferroelec. Freq. Contr.*, vol. 63, no. 1, pp. 60–71, 2016.
[30] J. A. Jensen, H. Bouzari, and M. B. Stuart, "Three-dimensional (3-D) imaging with a row-column addressed (RCA) transducer array using synthetic aperture sequential beamforming (SASB)." Patent US 2018 / 0348624 A1, December 2018.
[31] T. L. Christiansen, M. F. Rasmussen, J. P. Bagge, L. N. Moesner, J. A. Jensen, and E. V. Thomsen, "3-D imaging using row–column-addressed arrays with integrated apodization — part II: Transducer fabrication and experimental results," *IEEE Trans. Ultrason. Ferroelec. Freq. Contr.*, vol. 62, no. 5, pp. 959–971, 2015.
[32] M. Flesch, M. Pernot, J. Provost, G. Ferin, A. Nguyen-Dinh, M. Tanter, and T. Deffieux, "4D in vivo ultrafast ultrasound imaging using a row-column addressed matrix and coherently-compounded orthogonal plane waves," *Phys. Med. Biol.*, vol. 62, no. 11, pp. 4571–4588, 2017.
[33] J. Sauvage, M. Flesch, G. Ferin, A. Nguyen-Dinh, J. Poree, M. Tanter, M. Pernot, and T. Deffieux, "A large aperture row column addressed probe for in vivo 4D ultrafast Doppler ultrasound imaging," *Phys. Med. Biol.*, vol. 63, pp. 1–12, 2018.
[34] J. Sauvage, J. Porée, C. Rabut, G. Férin, M. Flesch, B. Rosinski, A. Nguyen-Dinh, M. Tanter, M. Pernot, and T. Deffieux, "4D functional imaging of the rat brain using a large aperture row-column array," *IEEE Trans. Med. Imag.*, vol. 39, pp. 1884–1893, June 2020.
[35] H. Bouzari, M. Engholm, S. I. Nikolov, M. B. Stuart, E. V. Thomsen, and J. A. Jensen, "Imaging performance for two row-column arrays," *IEEE Trans. Ultrason. Ferroelec. Freq. Contr.*, vol. 66, no. 7, pp. 1209–1221, 2019.
[36] S. Holbek, T. L. Christiansen, M. B. Stuart, C. Beers, E. V. Thomsen, and J. A. Jensen, "3-D vector flow estimation with row-column addressed arrays," *IEEE Trans. Ultrason. Ferroelec. Freq. Contr.*, vol. 63, no. 11, pp. 1799–1814, 2016.
[37] M. Schou, L. T. Jørgensen, C. Beers, M. S. Traberg, B. G. Tomov, M. B. Stuart, and J. A. Jensen, "Fast 3-D velocity estimation in 4-D using a 62 + 62 row-column addressed array," *IEEE Trans. Ultrason. Ferroelec. Freq. Contr.*, vol. 68, no. 3, pp. 608–623, 2020.
[38] L. T. Jørgensen, M. Schou, M. B. Stuart, and J. A. Jensen, "Tensor velocity imaging with motion correction," *IEEE Trans. Ultrason. Ferroelec. Freq. Contr.*, vol. 68, no. 5, pp. 1676–1686, 2020.
[39] J. A. Jensen, "Field: A program for simulating ultrasound systems," *Med. Biol. Eng. Comp.*, vol. 10th Nordic-Baltic Conference on Biomedical Imaging, Vol. 4, Supplement 1, Part 1, pp. 351–353, 1996.
[40] J. A. Jensen and N. B. Svendsen, "Calculation of pressure fields from arbitrarily shaped, apodized, and excited ultrasound transducers," *IEEE Trans. Ultrason. Ferroelec. Freq. Contr.*, vol. 39, no. 2, pp. 262–267, 1992.
[41] L. T. Jørgensen, M. B. Stuart, and J. A. Jensen, "Transverse oscillation tensor velocity imaging using a row-column addressed array: Experimental validation," *Ultrasonics*, pp. 1–1, 2023.
[42] C. Kasai, K. Namekawa, A. Koyano, and R. Omoto, "Real-Time Two-Dimensional Blood Flow Imaging using an Autocorrelation Technique," *IEEE Trans. Son. Ultrason.*, vol. 32, no. 3, pp. 458–463, 1985.